

Whole-Brain Activity Maps Reveal Stereotyped, Distributed Networks for Visuomotor Behavior

Ruben Portugues,^{1,3,4} Claudia E. Feierstein,^{2,4} Florian Engert,¹ and Michael B. Orger^{2,*}

¹Department of Molecular and Cellular Biology, Harvard University, 16 Divinity Avenue, Cambridge, MA 02138, USA

²Champalimaud Neuroscience Programme, Avenida Brasília, Doca de Pedroços, Lisbon 1400-038, Portugal

³Present address: Max Planck Institute of Neurobiology, Am Klopferspitz 18, 82152 Martinsried, Germany

⁴These authors contributed equally to this work

*Correspondence: michael.orger@neuro.fchampalimaud.org

<http://dx.doi.org/10.1016/j.neuron.2014.01.019>

SUMMARY

Most behaviors, even simple innate reflexes, are mediated by circuits of neurons spanning areas throughout the brain. However, in most cases, the distribution and dynamics of firing patterns of these neurons during behavior are not known. We imaged activity, with cellular resolution, throughout the whole brains of zebrafish performing the optokinetic response. We found a sparse, broadly distributed network that has an elaborate but ordered pattern, with a bilaterally symmetrical organization. Activity patterns fell into distinct clusters reflecting sensory and motor processing. By correlating neuronal responses with an array of sensory and motor variables, we find that the network can be clearly divided into distinct functional modules. Comparing aligned data from multiple fish, we find that the spatiotemporal activity dynamics and functional organization are highly stereotyped across individuals. These experiments systematically reveal the functional architecture of neural circuits underlying a sensorimotor behavior in a vertebrate brain.

INTRODUCTION

How do networks of interconnected neurons in the brain process sensory information and generate appropriate actions? Efforts to answer these questions for small circuits in invertebrates, whose wiring diagram is often already known, have highlighted the crucial importance of recording activity dynamics during natural behavior for identifying the functional roles of individual neurons (Selverston, 2010; Alivisatos et al., 2012; Bargmann and Marder, 2013). Advances in imaging technology, including the development of sensitive genetically encoded calcium indicators (Akerboom et al., 2012; Chen et al., 2013b), have opened up the possibility of simultaneous and systematic recording from large populations of neurons. Recording from restrained but behaving animals is a powerful way to simultaneously measure neural activity and acquire high-resolution, quantitative measurements of behavior (Georgopoulos et al., 1986; Lisberger, 1988; Dombeck

et al., 2007; Chiappe et al., 2010; Maimon et al., 2010). In the small, transparent zebrafish larva, it is possible to both noninvasively record activity throughout the whole brain with single-cell resolution (Friedrich et al., 2010; Ahrens et al., 2012; 2013) and also reliably elicit and measure behavior in head-restrained individuals (Portugues and Engert, 2011; Miri et al., 2011a). This enables unbiased identification of neurons with particular activity patterns or behavioral functions.

The optokinetic response (OKR) is a reflexive behavior, found in virtually all vertebrates, which consists of a rotational movement of the eyes in response to whole-field rotational motion that serves to reduce image motion on the retina (Walls, 1962; Huang and Neuhauss, 2008). In zebrafish larvae, the response appears reliably at an early age (Easter and Nicola, 1997; Beck et al., 2004) and has been used in genetic screens to identify mutations affecting several aspects of visual system development and function (Brokerhoff et al., 1995, 1997; Neuhauss et al., 1999; Muto et al., 2005) and as a model to study human oculomotor disorders (Maurer et al., 2011). A wealth of data from electrophysiological and anatomical studies has identified several brain areas and pathways carrying sensory and motor signals relevant to the OKR (Büttner-Ennever and Horn, 1997; Masseck and Hoffmann, 2009). Nevertheless, it is striking that there is no clear consensus as to how and where neurons in the zebrafish brain are active during this simple behavior. This problem stems in part from the difficulty of integrating data recorded from small groups of neurons in different brain areas and across diverse species, where the anatomical correspondence of structures, and functional conservation, from the brain of one animal to another is not always clear. Establishing a rapid and unbiased way to systematically identify the active neurons, and the signals they are carrying, in an individual behaving animal is a crucial step toward solving this problem.

Here, we present whole-brain maps of activity dynamics recorded using two-photon calcium imaging from individual zebrafish while they perform the OKR. We compare the spatio-temporal structure of this activity across individuals and show that the network can be dissected into highly stereotyped distinct functional modules based on correlation with a broad set of behavioral parameters. This provides important constraints on the circuit that mediates the OKR, sheds lights on the functional architecture of visuomotor processing in the brain, and paves the way for targeted experiments aimed at unraveling how this circuit works.

RESULTS**Whole-Brain Imaging of Neuronal Responses during OKR**

We used two-photon microscopy to image larval zebrafish with panneuronal expression of the genetically encoded calcium indicator GCaMP5G (Experimental Procedures; Akerboom et al., 2012). Larvae were restrained in agarose, and the agarose removed from the eyes and tail to allow for unimpeded movement. To elicit the OKR, we projected sinusoidally rotating, whole-field visual stimuli on a screen below the fish (Figure 1A), which reliably evoked conjugate horizontal eye movements (Beck et al., 2004; Huang and Neuhauss, 2008). These OKRs consisted mainly of slow tracking movements phase-locked to the stimulus and were accompanied by occasional fast reset saccades and swims (Figure 1B; Figure S1A available online; Movie S1). Eye and tail movements in response to visual stimulation were recorded using an infrared-sensitive camera (Figure 1A). Because the tracking responses persisted robustly for many hours (Figure S1B), we were able to systematically image, under comparable behavioral conditions, the majority of the brain (Figure 1C) of individual fish with a voxel spacing of less than 1 μm in all three dimensions.

Dynamics and Spatial Distribution of Neuronal Activity during OKR

Stimulus-locked, phasic activity was evident in areas throughout the brain, including both cell somata and neuropil regions (Movie S2). To analyze the activity dynamics across different brain areas, we designed an automated algorithm to segment the image into regions of interest (ROIs) by assigning voxels to ROIs based on their correlations with neighboring voxels (see Supplemental Experimental Procedures). Because, for most ROIs, fluorescence changes occurred at the stimulus frequency (Movie S2), we first focused our analysis on the temporal relationship between ROI activity and stimulus. To visualize the whole-brain activity dynamics, we assigned each ROI a hue based on the timing of its response relative to the stimulus (Figure S2), with intensity representing the relative power at the stimulus frequency (dorsal view, Figure 1D; other views, Movie S3). We observed that the neural activity pattern showed a complex but markedly ordered distribution, which is repeated symmetrically on both sides of the brain, with corresponding regions on opposite sides active in antiphase (Figure 1D). The consistent structure of this pattern is evident when the map is flipped left to right and phase-shifted by 180° (Figure 1D, bottom).

Activity locked to the stimulus was found throughout the brain, particularly in the optic tectum and pretectum, cerebellum, habenulae, and throughout the caudal brainstem. Dividing up the ROIs by brain area (Movie S4), we found roughly equal numbers on the left and right in each region. A notable exception was the dorsal habenula, a region known to have pronounced anatomical asymmetry (Bianco and Wilson, 2009), where we found responses predominantly on the left side (Figures 1D and 1E). The activity in the habenula, as well as in the torus longitudinalis, showed a distinct temporal pattern from the rest of the network and may relate to the light/dark structure of the pro-

jected stripe pattern, rather than the visual motion signals that drive the OKR.

Many ROIs align with individual cell somas (Figure 1D, panel i), whereas some are localized to synaptic regions, such as thin stripes in the superficial layers of the tectum (Figure 1D, arrowhead in panel ii), which are likely to be the axon terminals of direction-selective retinal ganglion cells (Gabriel et al., 2012; Nikolaou et al., 2012). Large domains of activity in neuropil are seen in the pretectal/thalamic retinal arborization areas (Figure 1D, panels i and iii) and two areas in the ventral hindbrain (Figure 1D, panel iv). Visual input from the retina reaches the brain through ten retinal arborization fields (AFs) (Burrill and Easter, 1994); however, it is not known which of these AFs are part of the OKR circuit. AF6 has been proposed to correspond to the mammalian nucleus of the optic tract (Roeser and Baier, 2003), but the *dark half* mutant, which lacks AF6 and other ventral tract AFs, has an intact OKR (Muto et al., 2005). We observed a large domain of activity spanning from AF4 to AF6 along the rostrocaudal axis and extending dorsally to the most rostral portion of AF9, suggesting the possibility that multiple redundant pathways exist to carry visual information for the OKR. In the dorsal medulla, we observed that activity has a columnar structure (Figure 1D, panel v), with interleaved regions active at opposite stimulus phases, which is interesting in light of the fact that this region is known to be organized into stripes of neurons with different projection patterns and neurotransmitter types (Kinkhabwala et al., 2011). It would be interesting to determine if the functional segregation we observe coincides with the anatomical organization described.

To further characterize the response dynamics, we looked at the distribution of phases at which the activity peaked for all active voxels (Figure 1F). This distribution showed four major peaks, with responses on both sides of the brain occurring mainly during ipsilateral nasal-to-temporal (ipsiversive) stimulus motion (Figure 1F). Activity was clustered in a narrow range of stimulus phases encompassing the time between maximum stimulus velocity and maximum eye position (Figure 1F). Responses in areas associated with sensory processing, such as the tectal neuropil, pretectum, and inferior olive, tended to precede activity in motor structures in the hindbrain (Figure 1G). Most areas, including the pretectum and inferior olive, contained regions active in phase with ipsiversive rotation, although the cerebellum showed the opposite pattern, consistent with crossed projections from the inferior olive (Straka et al., 2006). The activity observed in the pretectum is consistent with recordings from the homologous region in mammals, the nucleus of the optic tract (NOT), that show selectivity for ipsiversive movement (Collewijn, 1975a).

Clustering of the raw traces, based on their temporal profiles, confirms the division of activity into four laterally symmetric, early and late clusters (Figure 2A). Four clusters of activity with similar profiles were found in every fish with a robust OKR (Figure S3). Based on their anatomical localization (Figures 2B and 2C) and their temporal order (Figure 2A), these clusters likely represent a division of the circuit into distinct sensory and motor domains, with the two structures repeated bilaterally.

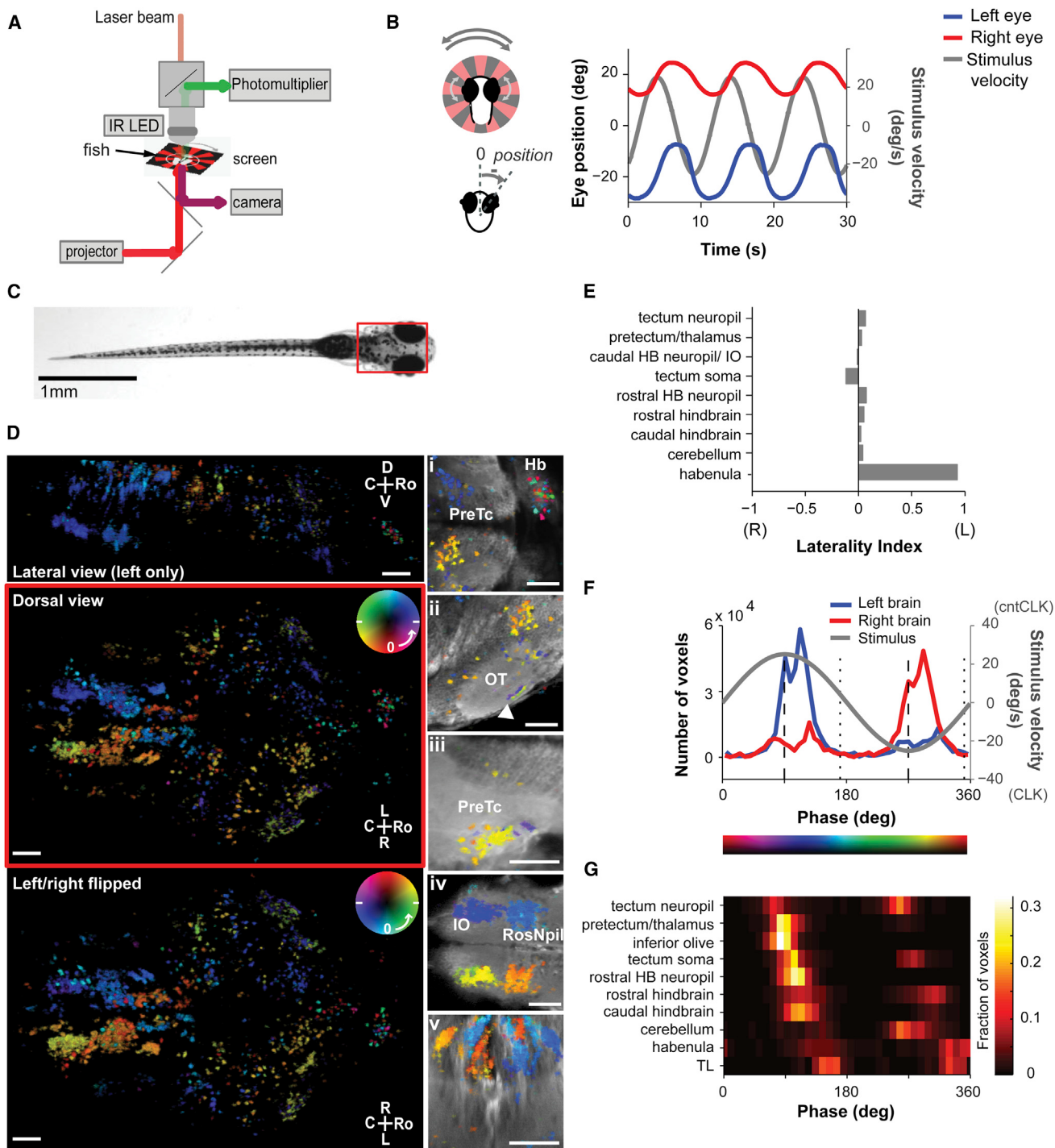


Figure 1. Imaging the Whole Brain of a Single Fish during Visuomotor Behavior

(A) Experimental setup. Zebrafish larvae were restrained in agarose, with their eyes and tail free, and placed on a screen for visual stimulation. Eye and tail movements were tracked while imaging brain activity with a two-photon microscope.

(B) Optokinetic response (OKR). Top left: larvae were presented with a rotating radial striped pattern. Bottom left: eye position was defined as the eye angle relative to the midline. Counterclockwise eye positions were defined to be positive. Right: larvae tracked the movement of the grating with a conjugate movement of the eyes. Stimulus rotation was sinusoidally modulated (gray, stimulus velocity). The mean eye position throughout the recording session is shown. In each imaging plane, the stimulus was presented three times. See also [Figure S1A](#) and [Movie S1](#).

(C) Image of a 6-day-old larval zebrafish. Red box indicates the imaged area in (D). Scale bar, 1 mm.

(legend continued on next page)

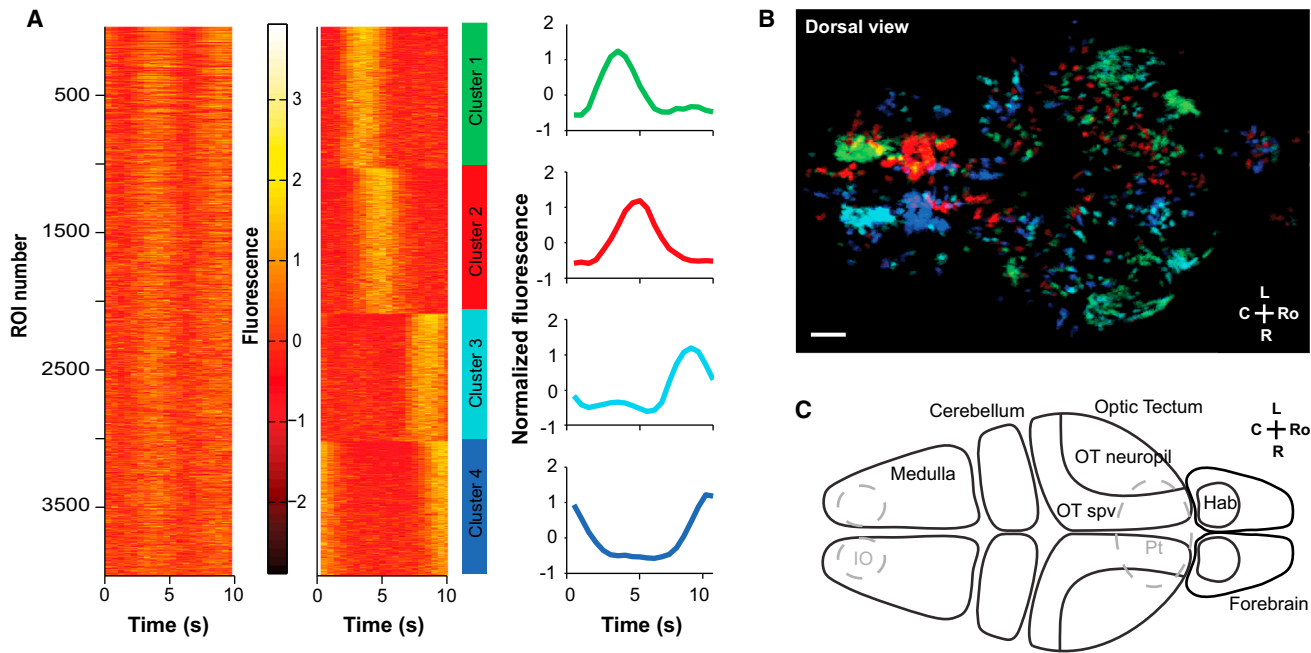


Figure 2. Clustering of Fluorescence Traces Reveals Four Temporal Clusters

(A) Activity traces of all ROIs can be grouped in four clusters. Left: activity for all ROIs of a fish (in rows); for each ROI, the normalized, average activity across all stimulus repetitions is shown. Center: ROIs sorted according to the cluster they fall into. Right: average of the Z score traces for each cluster. See also [Figure S3](#).

(B) Anatomical distribution of activity clusters in one fish. Sum projection showing the distribution of the four clusters of activity in the same fish as in (A), with colors corresponding to the color traces in (A). Scale bar, 50 μ m.

(C) Schematic outlining relevant brain regions in the zebrafish larvae, in a dorsal view. OT, optic tectum; OT spv, optic tectum stratum periventriculare; IO, inferior olive; Pt, pretectal area; Hab, habenula. Gray dashed lines demarcate areas located more ventrally.

Neuronal Responses during OKR Are Left-Right

Symmetric and Highly Stereotyped across Fish

In order to identify regions that were consistently activated during the OKR and to quantify the stereotypy of the spatiotemporal pattern of activity, we compared the whole-brain activity maps across multiple fish. To that end, data from each fish were registered in three dimensions to a reference brain ([Figure 3A](#)) (Rohlfing and Maurer, 2003; Jefferis et al., 2007), with a registration accuracy on the order of one cell soma diameter ($4.5 \pm 0.5 \mu\text{m}$; see [Experimental Procedures](#)). [Movie S5](#) shows how the ROI maps across two or more fish were aligned and averaged to reveal a core set of three-dimensional structures that were reliably activated. We first quantified the degree of similarity across

fish by calculating the probability of finding an ROI in each registered voxel. Many voxels showed activity in nearly every fish tested ([Figure 3B](#)). To assess the stereotypy of the temporal structure of the responses, we asked how far, on average, you have to travel from any active region to find a region with similar activity in another fish (see [Experimental Procedures](#)). For most ROIs, this distance was less than 15 μm , and, in an extensive network throughout the brain, especially in the hindbrain and neuropil regions around the retinal arborization fields, it was less than 2 μm ([Figures 3C and 3E](#)), which is on the scale of a single cell soma in the larval fish brain and at the limit of our registration accuracy. The stereotypy and bilateral symmetry are particularly evident when we compare each fish's brain to a

(D) Activity phase maps show that different brain areas are modulated at different phases relative to the stimulus. Center left: rendered dorsal view of all ROIs in one fish, color-coded according to the phase of their response at the stimulus frequency (see [Experimental Procedures](#) and [Figure S2](#)); white marks in the color wheel show the peaks of stimulus velocity. Top left: lateral view of ROIs in the left half of the brain. Bottom left: dorsal view that has been left/right flipped, and the color map phase-shifted by 180 degrees, to illustrate the symmetry of responses in most brain regions. Right insets show zoomed-in views of ROIs overlaid on the average GCaMP5G fluorescence as an anatomical reference. (i)–(iv) are dorsal views, and (v) is a coronal view. (i) Habenula (Hb) and pretectum (PreTc). (ii) Cell somas in the optic tectum (OT) and layered responses in the neuropil (arrowhead). (iii) Pretectal retinal ganglion cell arborization areas. (iv) Inferior olive (IO) and rostral neuropil (RosNpil) in the hindbrain. (v) Cell columns in the hindbrain. Scale bars, 50 μm . See also [Movie S3](#).

(E) Laterality index for different brain areas. The habenula showed marked asymmetry, with most activity occurring on the left side. HB, hindbrain; TL, torus longitudinalis.

(F) Distribution of phases of activation for voxels located in the left (blue) and right (red) halves of the brain. Phases are corrected to account for the delay introduced by GCaMP5G. Bottom color bar shows the correspondence between phase and map color.

(G) Timing of activation across brain areas. Normalized histogram of the phases of peak activity for different brain areas. Left and right areas have been pooled with a 180° phase shift. Phases are corrected as in (F).

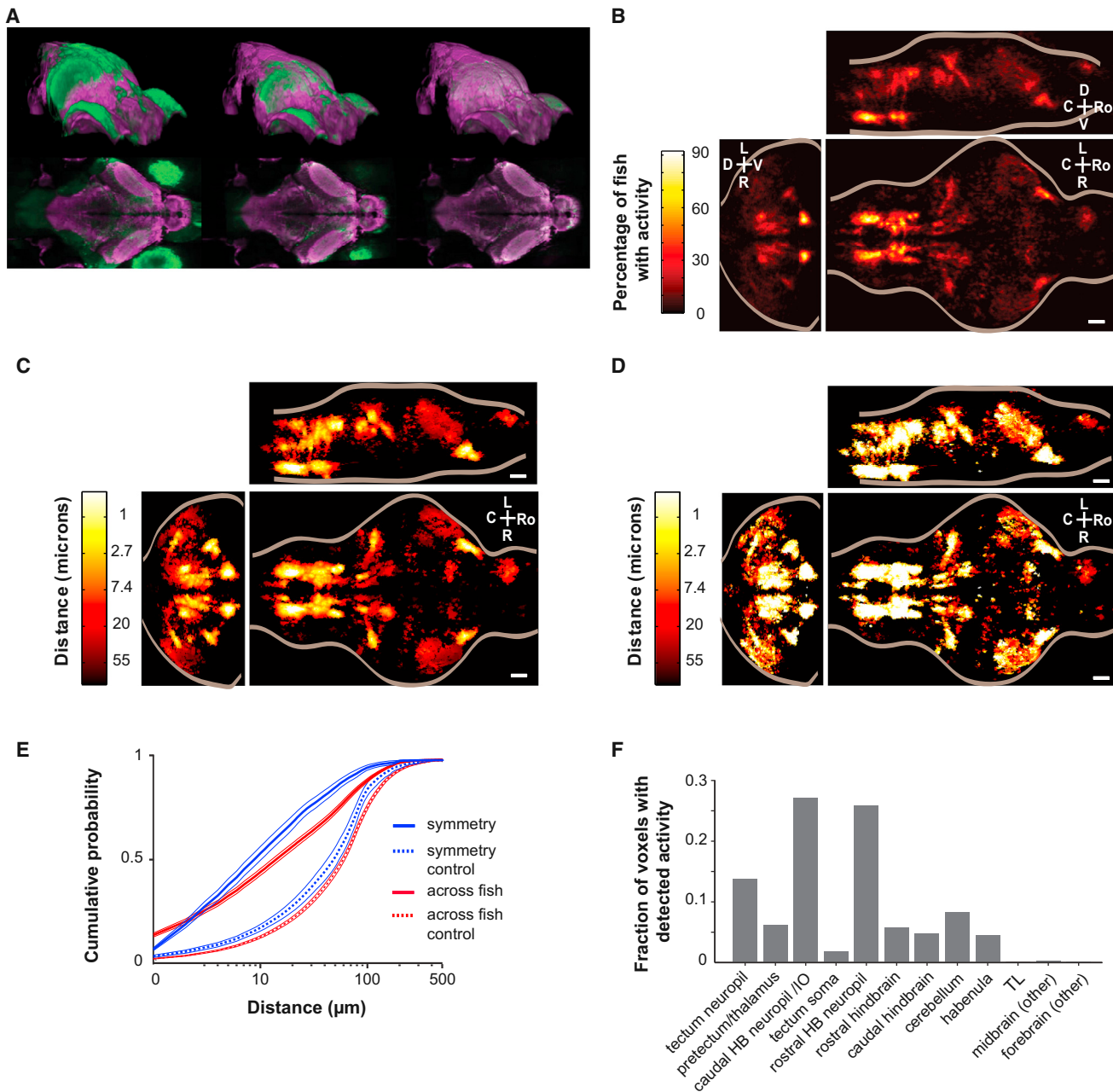


Figure 3. Morphing onto a Reference Brain Reveals Stereotypical Activity

- (A) An individual larva brain (green) is morphed in three dimensions onto a reference brain (magenta) by performing an affine followed by a nonrigid alignment.
- (B) Maximum projections from three orthogonal views, showing the percentage of fish ($n = 13$) imaged that show activity at each voxel (after registration) for all voxels within the brain. Scale bars in all panels, $50 \mu\text{m}$.
- (C) Minimum projections of the median distance that needs to be traveled in every other brain to find a similarly active voxel (see [Experimental Procedures](#)). The data are averaged across all comparisons ($n = 13$ fish, 156 comparisons).
- (D) Minimum projections of the median distance that needs to be traveled to find a similarly active voxel in the left/right flipped of the same brain. The data were averaged across all fish ($n = 13$).
- (E) The cumulative probability for finding a similarly active voxel within a given distance for the data in (C) (red) and (D) (blue). The data are averaged across all comparisons (red line, $n = 13$ fish, 156 comparisons). To control for the overall spatial distribution of ROIs, the same analysis was performed with the phases of the starting ROIs randomly shuffled (dotted lines).
- (F) Fraction of detected active voxels by brain region in imaging data averaged across three individual brains from fish that were selected based on similarity of behavioral profile during imaging.

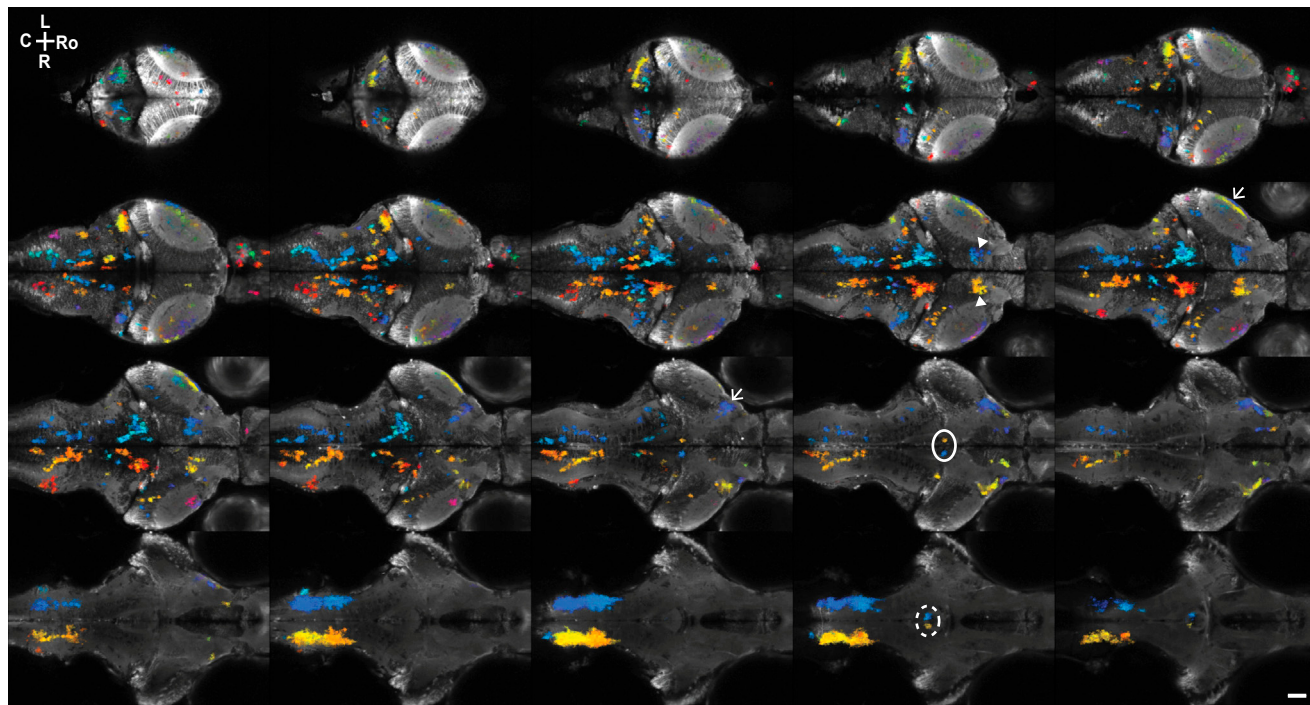


Figure 4. Averaging Raw Data from Morphed Brains Provides a Comprehensive Map of the Areas Active during Behavior

Color-coded activity phase of ROIs segmented from volumetric imaging data averaged across three fish. ROIs are superimposed on average GCaMP5G fluorescence for anatomical reference. Average planes are shown at 10 μm intervals from a stack of 510 image planes with 0.5 μm z-separation. Features highlighted are the oculomotor nucleus (solid line), the interpeduncular nucleus/median raphe (dashed line), the pretectum (arrowheads), and retinal ganglion cell arborization fields (arrows). See also Movies S6 and S7.

left/right-flipped version of the same brain, allowing for a 180-degree phase shift (Figure 1D, bottom panel). In this case, most ROIs are less than 10 μm away from a matching ROI on the opposite side (Figures 3D and 3E). Some cells in the left habenula still find matches, on a slightly longer spatial scale, due to small numbers of similarly responding cells in the right habenula. In the stratum periventriculare of the optic tectum, where a few active neurons are scattered within a dense layer of cell bodies, the precise location of the active somas was more variable from individual to individual (Movie S5).

Combining Data from Multiple Brains Gives an Average Activity Map

Taking advantage of this stereotypy, we averaged the raw pixel fluorescence data across fish to reveal structure in weakly active areas that lie below the detection threshold for individual fish. Combining data from three fish with closely matched behavior, we detected activity in 65% more voxels than the combination of the three individuals alone. In many places, the alignment is sufficiently precise to allow the identification of fiber tracts, based on functional signals, between active cell bodies and coactive neuropil regions (arrowhead, Movie S6). The resulting average activity map reveals a distributed network, consisting of fewer than 5% of all imaged voxels, but that nevertheless spans a large volume of the brain (Figure 3F; Movie S6). As expected, activity was evident in regions such as the oculomotor nucleus and multiple retinal projection fields, confirming the val-

idity of our activity maps (Figure 4; Movie S7). Surprising features are also revealed, such as left/right-alternating activity in neuropil in the vicinity of the interpeduncular nucleus or the closely associated median raphe (Figure 4), both of which receive bilateral innervation from the habenula (Aizawa et al., 2005; Amo et al., 2010).

Smooth Spatial Gradients in Activity Timing

Although activity in each region is concentrated around particular response phases, within most areas we observed smooth spatial gradients of activity timing, which either propagate along different anatomical axes or radiate from the center of active structures outward (Figure 5; Movie S8). Prominent examples included one group of pretectal neurons in which responses progress from rostral to caudal, whereas a distinct rostral sweep is seen in the cerebellar neuropil. Several such gradients are evident in structures throughout the hindbrain. These could result from gradients of physiological or tuning properties, as have been described in neurons in both the oculomotor integrator and spinal motor networks in zebrafish (McLean et al., 2007; Miri et al., 2011a), or from topography of local or interregion connectivity. These gradients could serve several functional purposes. Some may reflect signal transformations, such as integration of activity within areas. Smooth progressions of responses times could also permit specific sequencing of actions or provide a substrate for learning properly timed and coordinated responses (Mauk and Buonomano, 2004).

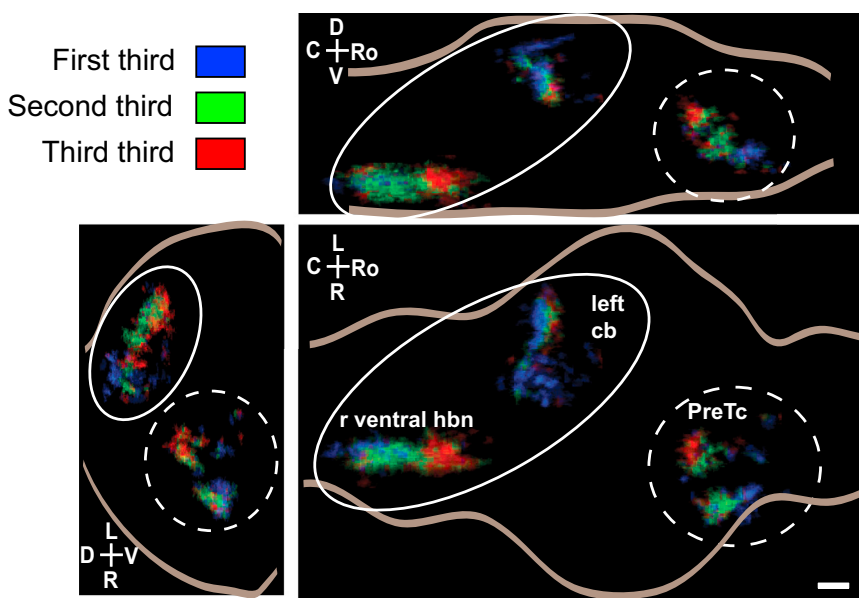


Figure 5. Spatial Gradients of Activity Timing Are Found in Various Brain Regions

Voxels were color-coded blue, green, or red depending on whether they fell into the first, second, or third third of voxels active within that region; that is, in each region, blue voxels were active before green voxels, which in turn were active before the red ones. A caudal-to-rostral gradient of activity timing is visible in the cerebellum (cb) and ventral hindbrain (r ventral hbn; only left cerebellum and contralateral hindbrain are shown for simplicity [solid line]), whereas a rostral-to-caudal gradient is observed in the preoptic/thalamus region (PreTc; only right is shown [dashed line]). Regions circled together were analyzed together; activity in the cerebellum (cb) and the contralateral inferior olive and more rostral neuropil show simultaneous activity. Only the cerebellum and preoptic region are displayed in the coronal projection for simplicity. Data are the average of three fish, as in Figure 4. See also Movie S8. Scale bar, 50 μ m.

Dissociating Sensory and Motor Signals in the Neuronal Responses

We hypothesized that the early and late response peaks in Figure 1F reflected processing of sensory and motor signals. However, when presented with motion throughout the visual field, fish moved both eyes together with similar amplitude and phase relative to the stimulus (Figure 1B; Figure S1A), making it hard to distinguish contributions of individual signals to the observed neural activity. To dissociate left and right eye and sensory and motor signals in different areas, we presented stimuli on the left or right side of the fish only, which causes different amplitude of motion of the two eyes, as well as in-phase and out-of-phase stimulation to both eyes that approximates translational motion and results in either conjugate eye rotation or vergence eye movements and optomotor swimming (Figure 6A; Figures S1C and S1D; Movie S9). In order to identify the sensorimotor signals represented in the activity of the ROIs, we correlated the measured fluorescence of every ROI with the predicted fluorescence time course arising from an array of different stimulus and behavioral parameters (Figure 6B; Figure S4) (Miri et al., 2011b).

Many active regions showed strong correlations with behaviorally relevant variables (Figure 6C; Figure S6). Some could be classified as carrying sensory signals relating to visual motion, such as stimulus velocity (Figures 6C and 6D; Figure S6), whereas others carried sensory information that was not directly related to the OKR. For example, many cells in the left dorsal habenula and torus longitudinalis were strongly modulated by the presence of the visual stimulus on one side or the other, probably encoding differential light levels between the two eyes (Figures 6C and 6D; Figure S5) (Northmore et al., 1983). Other regions, which we classified as motor, were correlated with eye and tail variables (Figures 6C and 6D). For instance, activity in ROIs clustered near the dorsal surface in the caudal hindbrain was strongly correlated with nasal-temporal positions of the ipsilateral eye (Figure 6C; Figures S5 and S6), which is consistent with responses found in area I cells in fish, which

form part of the horizontal velocity-to-position integrator (Pastor et al., 1994). Other regions were correlated with more complex combinations of sensorimotor variables. Responses of many tectal neurons were inhibited in a direction-selective manner by stimuli presented to the ipsilateral side (Figures 6C and 6D; Figures S5 and S6). They responded much more strongly when motion was presented in opposite rotational senses to both eyes, which is consistent with translational movement through the water (Frost et al., 1990), than when whole-field rotational motion was shown. Thus, these neurons are unlikely to be directly involved in the OKR, which is in agreement with previous ablation studies (Roeser and Baier, 2003). Conversely, neurons in some hindbrain areas were selective for whole-field rotating stimuli and unresponsive to whole-field translation motion stimuli (Figure 6C; Figures S5 and S6), suggesting that these neurons may be involved in the OKR.

Responses to Sensory and Motor Variables Are Localized to Defined, Stereotyped Brain Regions

We next analyzed the three-dimensional arrangement of the voxels correlated with these sensorimotor variables in order to identify different functional networks across the whole brain. To identify these structures in an unbiased way, we took fluorescence traces from overlapping cubes of approximately 5 μ m tiling the entire imaging volume, correlated each of these cubes with 191 different sensorimotor variables, and then aligned these correlation maps to the reference brain. Figure 7 shows the distributions of cubes whose activity best correlated with different parameters, summed across seven fish (Figure S7). Each signal localizes to one or a few distinct areas, which are similar between the left and right sides and align very well across different individuals (Figure 7). One exception to this pattern is the response to dimming on one side during hemifield stimulation. In this stimulus condition, cells in the left habenula are selective for both left and right side stimulation, whereas there is little activity in the right habenula. In addition, there is a striking asymmetry in

the ventral cerebellar area of the hindbrain, where a small area on the left is responsive during left stimulus presentation, whereas a more diffuse bilateral activation is observed during presentation on the right (Figure 7), suggesting different processing of information from the two eyes.

Individual regressors may not fully capture the functional properties of a given neuron. We hypothesized that a more accurate functional classification could result from analyzing the correlations with all relevant regressors, rather than the best individual fit. We therefore performed a k-means clustering analysis on the complete vectors of correlation coefficients for voxels from seven fish brains. Several symmetric pairs of functional clusters were found, some of which match very well to the single-parameter maps in Figure 7 (Figures 8A–8C; Figure S8; Movie S10). Others were not so clearly linked to a single variable but were broadly correlated with, for example, the left and right eye velocity and position signals that were consistent with clockwise or counterclockwise conjugate rotation. In addition, clear and consistent symmetrical structures associated with swimming activity could be extracted from individual fish, even though the average activity trace from this cluster was rather flat, because this behavior was poorly correlated across individuals, or across stimulus repetitions, under these conditions (Figures 8B and 8C). Some areas correlated with swimming also show strong correlations with other parameters, such as eye acceleration due to rapid eye movements that occur when swimming, and therefore may not all be grouped together based only on peak correlation value. The multidimensional clustering therefore gives a much more comprehensive map of this hindbrain locomotor network (compare Figures 7 and 8B with Figure S8).

DISCUSSION

Here, we have characterized neural activity dynamics at single-cell resolution throughout the entire brains of individual animals engaged in sensorimotor behavior. We have combined sensitive genetically encoded calcium indicators, the ability to monitor behavior and neural activity simultaneously, and a behavior that can be reliably and repetitively elicited to enable a systematic imaging approach. Our experiments reveal that network activity in the vertebrate brain during a simple behavior is sparse and widely distributed, but at the same time it shows a striking spatial organization and can be highly stereotyped on a micrometer scale across individuals. Clustering of activity patterns reveals distinct temporal profiles, which are confined to particular anatomical structures. Using different stimulus configurations that evoke distinct patterns of behavior, we identify areas associated with defined sensory and motor variables. This comprehensive map of activity during the OKR, although it does not, by itself, fully explain the neural basis of the behavior, places substantial constraints on the possible circuit mechanisms and will enable targeted recordings and manipulations to identify the functional roles of different areas.

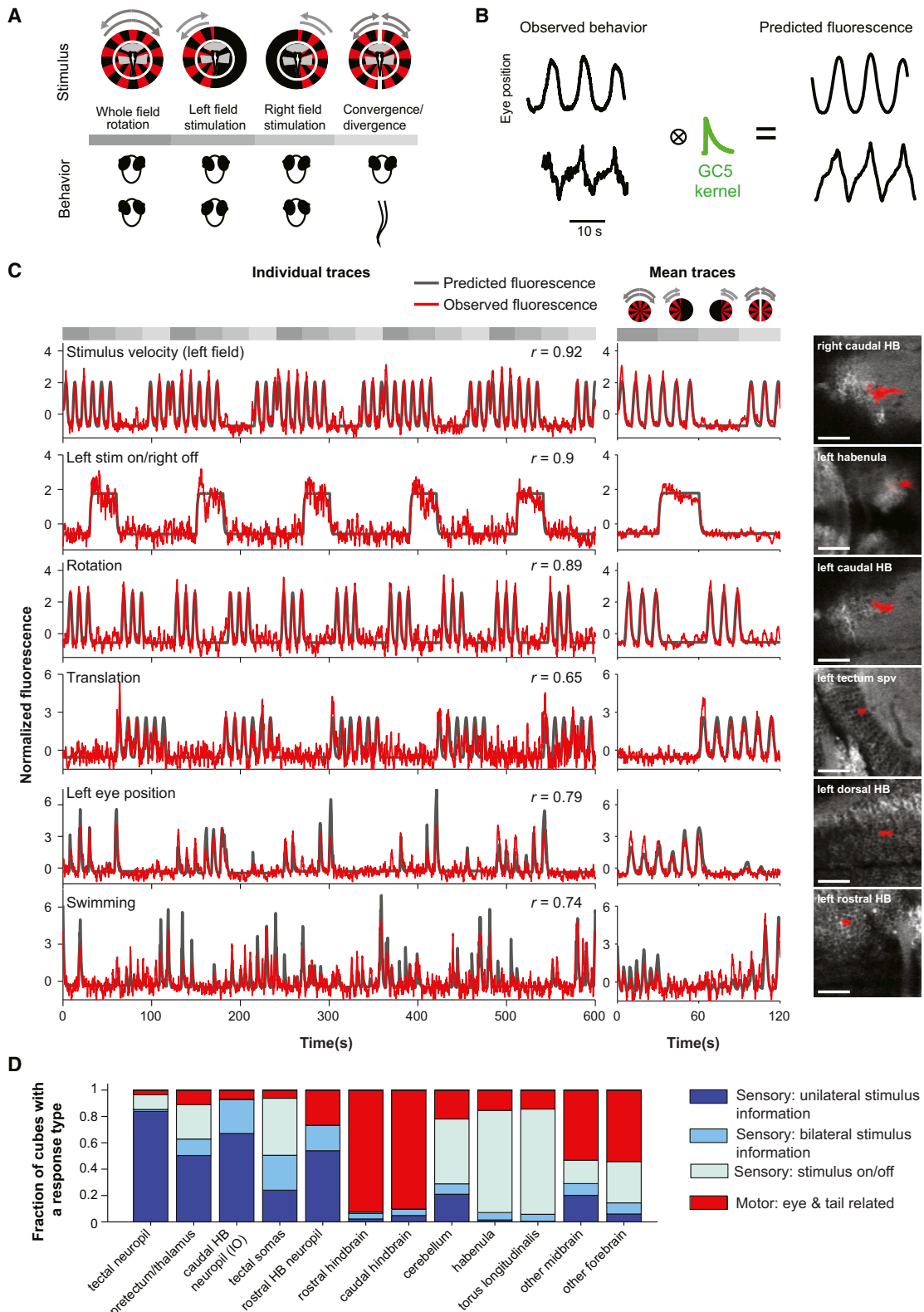
Our finding that a simple reflex activates such an elaborate and widely distributed network of neurons in the brain may seem surprising. The simplest circuit one could envisage for the OKR would involve connections from optic-flow-sensitive neurons in the pretectum to extraocular motor neurons (Figure 9),

and, indeed, evidence for such a direct pathway has been found in birds, amphibians, and also fish (Brecha and Karten, 1979; Cochran et al., 1984; Masseck and Hoffmann, 2009). However, such a simple solution is inadequate to account for the full complexity of the behavior: the OKR depends on the ability to combine information from both eyes, generate motor commands that take into account the current state of the system, adapt in response to feedback, and integrate with other behavioral systems that depend on shared circuitry for visual processing and motor output (Büttner and Büttner-Ennever, 2006). Below, we summarize our findings in the context of working hypotheses of these different functions of the OKR circuit.

Sensory Inputs

In our experiments using a sinusoidally modulated OKR stimulus, a large cluster of neurons in the pretectum showed responses in phase with temporal-to-nasal (TN) motion in the contralateral eye (e.g., Figures 1D [panels i and ii], 1G, and 4; Movie S6). Experiments in many different species have shown that sensory inputs to the horizontal OKR originate from ON-type, direction-selective retinal ganglion cells, which project to pretectal and accessory optic nuclei, in particular the NOT and dorsal terminal nucleus in mammals and the nucleus lentiformis mesencephali (LM) in other tetrapods (Oyster et al., 1972; Collewijn, 1975b; Soodak and Simpson, 1988; Büttner-Ennever and Horn, 1997; Masseck and Hoffmann, 2009). Similar to our observations, neurons in both these areas respond mostly to TN motion in the contralateral eye. In fish, two candidate nuclei were originally suggested as homologs of the LM and the accessory optic nucleus of the basal optic root (Finger and Karten, 1978), based on features of their projection patterns, but, more recently, others have proposed a single pretectal nucleus in fish, which contains neurons responding to all directions of motion (Klar and Hoffmann, 2002; Masseck and Hoffmann, 2009). The pronounced asymmetry in directional sensitivity that we find in our data may account for the observation that, in larval zebrafish, as in many species, TN motion drives stronger OKR than nasal-to-temporal (NT) motion (Roeser and Baier, 2003; Burgess et al., 2009) but does raise the question of how monocularly presented OKR stimuli can drive a response in both directions. Burgess et al. observed that *robo3* mutant zebrafish, which have impaired formation of commissures, have a specific deficit for NT motion in the monocular OKR and propose that NT motion acts by suppressing crossed inhibitory connections between pretectal nuclei (Burgess et al., 2009; Prochnow et al., 2007). Interestingly, here we find functional evidence for a crossed inhibitory pathway with a preference for TN motion in the responses of translation-sensitive neurons in the optic tectum (Figures 6C and 8). These respond in phase with contralateral NT motion, except when it occurs simultaneously with ipsilateral TN motion.

Responses to whole-field motion stimuli have previously been found in retinal ganglion cell terminals and neurons in the optic tectum of zebrafish larvae (Niell and Smith, 2005; Del Bene et al., 2010; Nikolaou et al., 2012). Similarly, we found signals in distinct, superficial layers of the tectum responsive to each of the two directions of motion (e.g., Figures 1D [panel ii] and 4), and, although most neurons in the large periventricular



(legend on next page)

layer did not show stimulus-locked responses, a substantial scattered population did, and could, in principle, be involved in driving the OKR. However, ablation studies in both zebrafish larvae and adult goldfish have indicated that the optic tectum is not required for this behavior (Springer et al., 1977; Roeser and Baier, 2003). It is striking that up to half of the tectal neurons that responded to visual stimuli in our experiments appear to integrate information from both eyes (Figures 6C, 6D, and 8), because their response to binocularly presented motion differed from the response to contralateral motion alone. In particular, responses to rotational motion stimuli were strongly suppressed. Although we are not aware of previous functional evidence for such neurons integrating binocular visual information in the tectum, anatomical tracing experiments have identified bilateral projections in mammals from the pretectum to the superior colliculus, the optic tectum homolog, and in vitro recordings have confirmed functional inhibitory connections (Baldauf et al., 2003; Born and Schmidt, 2004). The preference for NT motion suggests that they would respond strongly to reafferent motion signals during forward locomotion and could be involved in gating visual processing, or detecting the proximity of objects, during swimming. This scattered population represents a very small percentage of the neurons in the tectum, which, in the zebrafish larva, contains on the order of 10,000 cells, so these cells would only be rarely sampled in electrophysiological recordings, highlighting the potential of whole-brain imaging methods such as the one used in this study.

Sensorimotor Processing

In many species, retinal motion signals pass through two integration processes that generate both a stored representation of eye velocity (velocity storage mechanism [VSM]; Figure 9), which can serve to make the OKR robust to interruptions of sensory input, and a velocity-to-position neural integrator (VPNI), which generates eye position signals that are used to counteract elastic forces that pull the eye toward its resting position and to trigger fast reset saccades during optokinetic nystagmus. Although early experiments argued against the existence of velocity storage in larval zebrafish (Beck et al., 2004), more recently a VSM has been shown to exist in fish as early as 5 days postfertilization, but its presence was masked in previous experiments by the

rapid decay of the position integrator at this stage of development (Chen et al., 2013a). The VPNI has been investigated in larval zebrafish in the context of maintenance of eye position following spontaneous saccadic movements in the dark (Miri et al., 2011a, 2011b). Curiously, the neurons we observe with the strongest eye position correlations are distributed differently from those previously observed, occupying a more restricted volume at a more dorsal level. Nevertheless, the region we describe does still fall within the volume used for optogenetic localization of the VPNI (Miri et al., 2011a). This apparent discrepancy could be explained by the fact that the two experimental paradigms differ in both motor dynamics (saccades versus smooth movements) and sensory inputs (continuously varying motion versus darkness), and it will be interesting to investigate the activity across these populations during different behaviors.

Adaptive Mechanisms

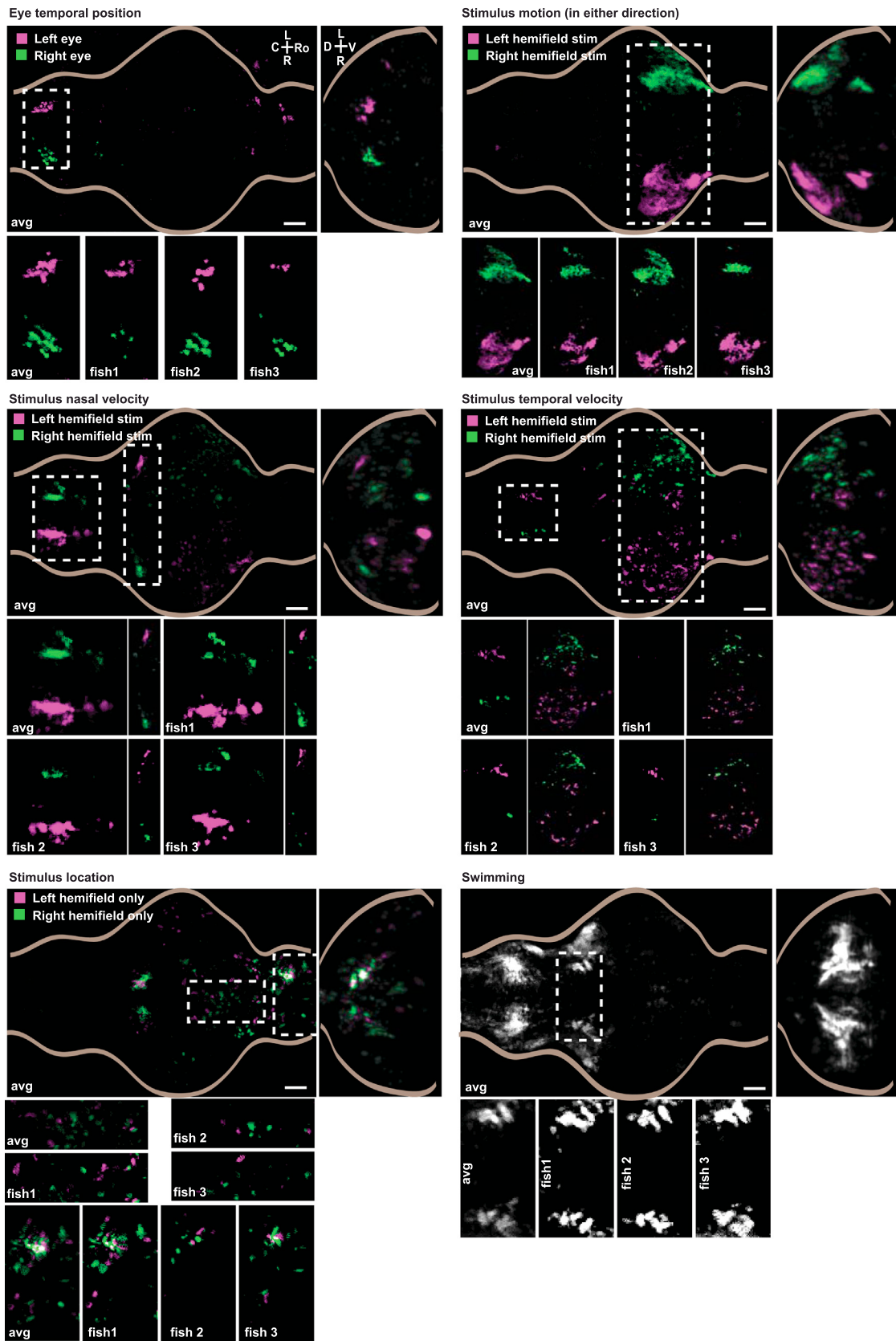
The OKR also shows learned adaptation driven by visual feedback, for which the cerebellum has been shown to be important (Nagao, 1983). The cerebellum receives OKR-related sensory and motor signals through mossy fibers and, in particular, retinal image motion signals via climbing fibers from the contralateral inferior olive, which in turn receive direct input from the pretectum. We observed a notable temporal gradient of activity timing in this olivocerebellar pathway during OKR (Figure 5; Movie S8), which could arise from spatial gradients of dynamics or velocity tuning and may provide a substrate for fine-tuning of the dynamics of adaptation. Although adaptation of the OKR has not been observed in larval zebrafish, rapid adaptation of the optomotor response, which depends on both cerebellar function and visual motion signals from the inferior olive, has been shown as early as 6 days postfertilization, suggesting that this circuit is functional even at early developmental stages (Portugues and Engert, 2011; Ahrens et al., 2012).

Stereotypy

Current attempts to map functional organization, or connectivity, of the brains of entire animals at cellular resolution raise the question of how similar such maps are across individuals. The correct approach to, and success of, proposed large-scale

Figure 6. Sensory and Motor Signals Are Reflected in the Measured Activity

- (A) Four stimuli were used to separate different sensorimotor signals: the standard rotating grating, rotating gratings presented on the left or right visual fields alone, and gratings rotating in opposite directions for each eye, to simulate forward and backward motion. Top: visual stimuli. Bottom: schematic of the behavior (eye rotation or tail movements) elicited. See also Figure S1B. Gray shades indicate the four stimuli periods.
- (B) Behavioral and stimulus-related variables were convolved with an exponential kernel using the decay time constant of GCaMP5G (Chen et al., 2013b). These convolved traces represented the predicted fluorescence that would be recorded if activity was related to each of those variables (see Experimental Procedures and Miri et al., 2011b). See also Figure S4.
- (C) ROI activity is strongly correlated with the predicted fluorescence for different behavioral variables (regressors). For each example ROI, the fluorescence trace and the predicted fluorescence for the regressor with the highest correlation are shown. Left: normalized (Z score) fluorescence traces for a subset of stimulus repetitions, and the corresponding normalized (Z score) behavioral trace. The correlation coefficient is indicated. Center: normalized average fluorescence across stimulus repeats (and planes) for the ROI, with the corresponding normalized average behavioral trace. A schematic of the four stimuli is shown above the top center plot. Gray boxes indicate the duration of each of the four stimuli in all plots. Right: anatomical localization of the ROIs (red). See also Figures S5 and S6. Scale bars, 50 μ m.
- (D) Sensory and motor variables are differentially represented in different brain areas. Fraction of cubes best correlated with different categories of regressors in different brain regions (best $r > 0.3$). Sensory variables were divided in three categories: one that included features related to stimulus motion, one that encompasses responses related to stimulus onset/offset, and another in which information was combined from the two eyes. Motor variables included those related to eye position or velocity and swimming.



(legend on next page)

projects to assemble brain-activity maps (Alivisatos et al., 2012) depends critically on the answer to this type of question. Previous studies in fruit flies have revealed anatomical stereotypy on the order of a few microns (Jefferis et al., 2007; Datta et al., 2008), but studies of neuromuscular connectivity in vertebrates found substantial variability (Lu et al., 2009). Meanwhile, in humans, spatiotemporal activity patterns from fMRI data have revealed similarities in processing of visual stimuli across individuals (Hasson et al., 2004). In this study, we have compared, across individual animals, neural circuit activity in the whole brain during behavior, with micrometer resolution. We find that a large part of the functional network active during the OKR is extremely stereotyped, such that it is possible to reliably predict the activity in individual voxels from their anatomical position alone. This has important practical consequences, because these areas can now be targeted, without further functional mapping, for ablations, electrophysiological recordings, optogenetics, or photoactivation, and also aligned with the scaffolds for existing anatomical atlases to find molecular markers for specific loci of activity (Ronneberger et al., 2012).

Whole-Brain Imaging

Although two-photon laser scanning microscopy offers many advantages for rapid, long-term volumetric functional imaging, especially during visual behavior (Renninger and Oger, 2013), alternative methodologies that offer different tradeoffs are advancing. Two recent studies in larval zebrafish used light-sheet imaging to image almost simultaneously from multiple z-planes (Panier et al., 2013; Ahrens et al., 2013). Scanned light-sheet imaging allows for the collection of many more voxels per unit time than standard two-photon microscopy, because an entire line, rather than a single point, is being exposed at any point in time. A disadvantage of the current plane-illumination methods, however, is that they require a constantly moving, visible laser passing laterally through the brain. This light may be sensed by the eye, which makes the study of visual responses more challenging, but could also produce responses directly through activation of light-sensitive areas in the brain (Fernandes et al., 2012; Kokel et al., 2013). Methods that combine two-photon excitation and plane illumination are a promising direction for the future. For example, wide-field two-photon excitation through temporal focusing was recently used to image simultaneously from much of the brain of *C. elegans* (Schrödel et al., 2013).

Whole-brain, single-cell-resolution functional maps as described here, especially when combined with connectivity maps and high-resolution anatomical atlases (Ronneberger et al., 2012; Arrenberg and Driever, 2013), have the power to reveal new functionally defined structures in the brain and provide a fundamental framework for understanding the complete neural circuits for behavior (Alivisatos et al., 2012).

Figure 7. Consistent Localization of Sensorimotor Signals in the Zebrafish Brain

Distribution of cubes that correlate best with particular sensory and motor variables ($r > 0.3$) averaged across seven fish. The location of many correlation-defined regions in the maps shows remarkable consistency across fish. For each regressor/regressor pair, a z-sum projection and a coronal sum projection are shown. Coronal sections were smoothed along the z axis with a $1.5 \mu\text{m}$ Gaussian filter. For each map, an area of interest is highlighted in the whole-brain map and a detailed view of this area is shown for the average map, alongside the identical region, in three example fish. See also Figure S7. Scale bars in all panels, $50 \mu\text{m}$.

EXPERIMENTAL PROCEDURES

Fish Care

Adult fish were maintained at 28°C on a 14:10 hr light cycle following standard methods. Larvae were raised in E3 embryo medium (5 mM NaCl, 0.17 mM KCl, 0.33 mM CaCl₂, and 0.33 mM MgSO₄). All procedures followed National Institutes of Health and the Portuguese Direcção Geral de Veterinária guidelines and were approved by the Standing Committees on the Use of Animals in Research of Harvard University and Champalimaud Foundation.

Calcium Imaging and Behavior Recording

Five- and six-day-old nacre (*mitfa*^{-/-}) elavl3:GCaMP5G zebrafish larvae were placed in a drop of 1.5% low-melting-temperature agarose in a Petri dish on a Sylgard 184 (Dow Corning) base and immersed in E3 solution. The agarose around the tail, caudal to the pectoral fins, as well as that in front of the eyes, was cut away with a fine scalpel to allow for movement. The dish was placed onto a light-diffusing screen and imaged on a custom-built two-photon microscope. A Ti-Sapphire laser (Spectra Physics Mai Tai) tuned to 950 nm was used for excitation. Larval brains were systematically imaged while larvae performed the OKR. Frames were acquired at 2 Hz in four, $0.83\text{-}\mu\text{m}$ -spaced interlaced scans, allowing each area of the brain to be evenly sampled at around 8 Hz. Visual stimuli, generated using LabView, were projected at 60 frames per second using a 3M MPro110 microprojector and a red long-pass filter (Kodak Wratten No.25) to allow for simultaneous imaging and visual stimulation. The stimulus consisted of radial light and dark stripes with a spatial period of 40 degrees (Movie S1). The stimulus position was rotated sinusoidally, centered on the fish, at 0.1 Hz with amplitude of 40 degrees. The focal plane was shifted by $0.5 \mu\text{m}$ every three stimulus repetitions. The fish were illuminated from above using a ring of infrared light-emitting diodes (850 nm wavelength) coupled to the objective. To track eye and tail movements, a small hole was cut in the diffusing screen to allow the fish to be imaged from below at up to 200 frames per second using an infrared-sensitive charge-coupled device camera (Pike F032B, Allied Vision Technologies). Tail and eye image data were streamed to hard disk using software written using National Instruments LabView.

Behavior Tracking and Analysis

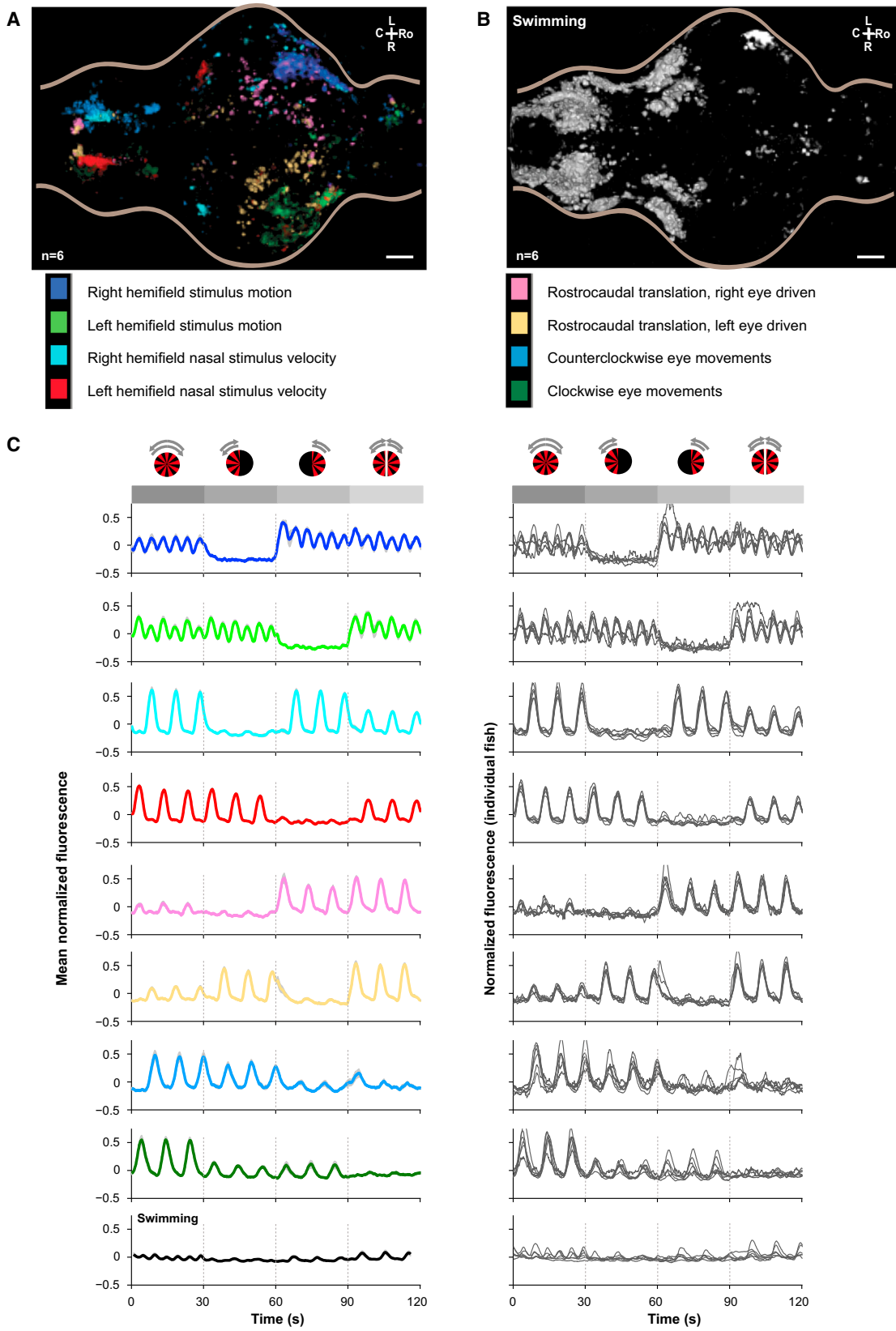
Eye angles and tail movements were tracked using custom routines in MATLAB (MathWorks). For details, see Supplemental Experimental Procedures.

Image Analysis

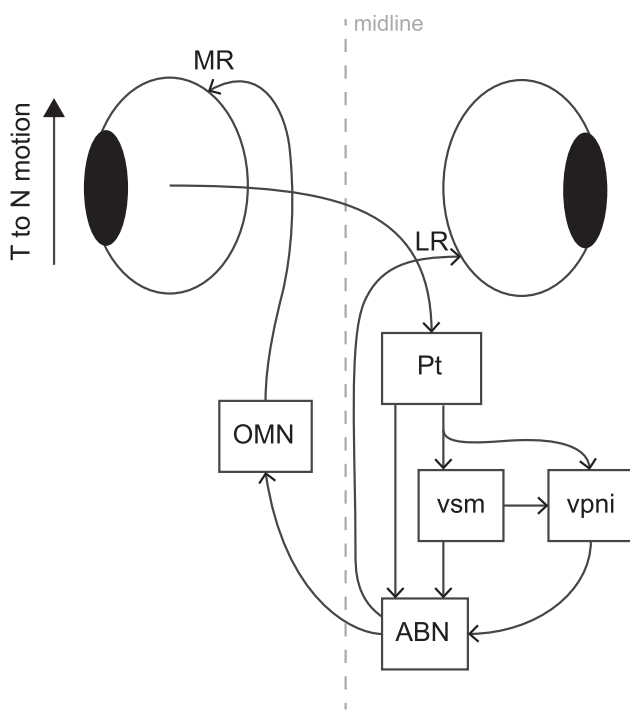
Image analysis was performed with MATLAB (MathWorks). To correct for drift or small movements of the fish, each image frame was aligned, using translation only, to the average image of that z-plane, and consecutive z-planes were aligned to each other with subpixel precision (Nestares and Heeger, 2000). Occasionally, vigorous swimming movements caused a large motion in a single frame. Such isolated frames that could not be aligned with a correction of less than two pixels were removed from analysis. ROI segmentation was performed using automated algorithms, based on local correlations between pixels (see Supplemental Experimental Procedures).

Anatomical Registration

Image registration was performed using the free Computational Morphometry Toolkit (CMTK; <http://www.nitrc.org/projects/cmtk/>) (Rohlfing and Maurer, 2003). For each fish, an anatomical stack was computed by summing the GCaMP5G fluorescence. One of the these stacks was chosen as the reference brain, and nonaffine volume transformations were computed to align each fish's anatomical stack to this reference stack using the *affine* and *warp* functions. These transformations were then used to transform individual



(legend on next page)

**Figure 9. Schematic Model for the OKR Circuit**

Temporal-to-nasal (T to N) motion to one eye is conveyed via direction-selective retinal ganglion cells to the contralateral pretectal area (Pt) and is relayed to extraocular motor neurons, either through a direct pathway or indirectly via circuits that implement a velocity storage mechanism (vsm) and velocity to position neural integrator (vpni). The abducens nucleus (ABN) drives ipsiversive eye movements via the lateral rectus muscle (LR) and sends projections, via internuclear neurons, to the contralateral oculomotor nucleus (OMN) to drive contraversive movements of the stimulated eye via the medial rectus muscle (MR).

ROIs from each fish into the frame of reference of the reference brain, allowing us to compare the anatomical location of ROIs from different fish. The precision of the registration was evaluated by selecting salient anatomical features, identifying them in every fish, and checking how closely they were transformed to the equivalent feature in the reference brain. Before transforming, the average distance between the features in individual and reference brain was $48.3 \pm 4.7 \mu\text{m}$ (mean \pm SEM). After transforming, the distance between the features in the transformed brains and the reference brain was $4.5 \pm 0.5 \mu\text{m}$.

Data Analysis

The phase of a particular ROI's activity relative to the stimulus was determined by taking the Fourier transform of the Z score of its fluorescence trace and determining the phase of the 0.1 Hz component. To make color-coded images, each ROI was assigned a hue, based on its phase, from the MATLAB hue saturation value color map and a value proportional to the amplitude of the 0.1 Hz component, reflecting how much modulation in that ROI was at

the stimulus frequency (Figure S2). Different anatomical regions were defined manually in the reference brain (Movie S4). For reasons of symmetry, when analyzing the phase distribution in particular anatomical regions, a phase shift of 180° was applied to all the ROIs from the right brain before pooling with the ROIs from the left brain. The laterality index was calculated using the formula $(\text{voxL} - \text{voxR})/(\text{voxL} + \text{voxR})$, where voxL and voxR are the number of voxels found in ROIs detected on the left and right of the brain, respectively. Cluster analysis of the traces was performed on individual fish using the k-means method. The optimal number of clusters was selected by inspection of silhouette plots for different even numbers of clusters (Figure S3). Reliability of finding activity in different areas (Figure 3B) was measured by the percentage of fish, following alignment, with ROIs including each voxel. The spatial scale of stereotypy was measured by asking, for every voxel in every ROI in every fish, how far you have to go, in all fish, to find a voxel that is active within 18° of the same stimulus phase (Figure 3C). To assess symmetry, we asked how far you need to go in a reference-aligned, left/right-flipped version of the same brain to find an ROI within 18° of the opposite stimulus phase. To control for the overall spatial distribution of ROIs, the same analysis was performed with the phases of the starting ROIs randomly shuffled. Three-dimensional renderings were performed using the ImageJ 3D Viewer plugin.

Regressors and Correlation Analysis

Regressors for correlation analysis were constructed from a set of 191 behavioral and stimulus-related variables (e.g., position and velocity of the eyes, stimulus velocity, onset/offset of stimuli). These were convolved with a kernel with an exponential decay based on the measured half-decay time for GCaMP5G (0.667 s) (Chen et al., 2013b) to produce a set of predicted fluorescence traces (Miri et al., 2011b) (Figure 6B; Figure S4) and were compared with the measured fluorescence traces by correlation. The interlaced scan waveform meant that each frame was scanned in four, slightly offset frames. Therefore, any ROI that spanned at least four adjacent scanned lines was partially imaged in each one of these four frames. Raw fluorescence traces were deinterlaced, by considering the voxels in each of these four subframes independently, to yield fluorescence traces at 8 Hz and smoothed with a 1.125 s width boxcar filter prior to correlation. For Figure 6C, correlation analysis was performed for automatically segmented ROIs to identify the variable that best described the signal of individual ROIs. For Figures 6D, 7, and 8, systematic correlation analysis was performed on cuboidal ROIs of $8 \times 8 \times 9$ voxels (roughly $6.6 \times 6.6 \times 4.5 \mu\text{m}$), tiling the brain in steps of 2 (x,y) or 3 (z) voxels. To assign voxels to a particular functional group, we required a threshold of at least 0.3 for the best absolute correlation coefficient. Based on comparisons with shuffled sets of regressors, this level of correlation rarely arises by chance and is therefore a conservative choice for detecting voxels with behavioral correlation (Figure S7A). At the same time, the precise threshold chosen is not critical to the set of areas identified (Figure S7B). Because the maximum r value depends on the original choice of regressors, it remains possible that new functional groups may be identified through better identification of appropriate regressors as well as by indicators, or fish lines, that offer better signal to noise in particular cell types. For Figure 8, clusters of correlation patterns were found as follows. First, the set of correlations with all behavioral regressors was calculated for all cuboidal, tiled ROIs across seven fish brains, and all those in which one regressor had a correlation of at least 0.3 were pooled (1,283,831 ROIs). Principal component analysis was applied to the data set, and k-means clustering was performed on the data projected onto the first ten components. Different numbers of clusters were tested, and the number of 25 clusters was selected manually because it gave the clearest separation of functional classes. Clustering

Figure 8. Functional Dissection of Activity Based on Multidimensional Clustering

(A) Rendered dorsal view of the anatomical distribution of four symmetrical functional clusters, averaged over seven fish, from k-means clustering of the behavioral correlation vectors of responsive cubes. See also Figure S8 and Movie S10.
 (B) Rendered dorsal view of the combination of five symmetric clusters that show strong correlation with tail movement, averaged over seven fish.
 (C) Fluorescence traces for each of the nine cube cluster groups shown in (A) and (B) for individual fish (right) and averaged across the seven fish (left; gray shading represents SEM). A schematic of the four stimuli is shown (see Figure 6 and Figure S1). Gray boxes and dotted lines indicate the duration of each of the four stimuli in all plots.

with larger numbers produced inconsistent fracturing of anatomical structures or segregation of clusters across fish, suggesting that true functional classes were being artificially divided.

Requests for data should be addressed to the corresponding author.

SUPPLEMENTAL INFORMATION

Supplemental Information includes Supplemental Experimental Procedures, eight figures, and ten movies and can be found with this article online at <http://dx.doi.org/10.1016/j.neuron.2014.01.019>.

AUTHOR CONTRIBUTIONS

R.P., C.E.F., F.E., and M.B.O. conceived the project; R.P., C.E.F., and M.B.O. carried out the imaging experiments and analyzed the data; and R.P., C.E.F., F.E., and M.B.O. wrote the paper.

ACKNOWLEDGMENTS

We are grateful to Loren Looger for sharing the GCaMP5G construct before publication, Kuo-Hua Huang for providing the objective-mounted infrared illuminator, and Torsten Rohlfing for assistance with implementation of the CMTK library. We thank Megan Carey, Christian Machens, Eugenia Chiappe, and Markus Meister for helpful comments on the manuscript. M.B.O. was supported by Marie Curie Career Integration Grant PCIG09-GA-2011-294049. C.E.F. was supported by a postdoctoral fellowship from the Fundação para a Ciência e a Tecnologia. F.E. was supported by National Institutes of Health grants DP1-NS082121 and R01-DA030304.

Accepted: December 24, 2013

Published: March 19, 2014

REFERENCES

- Ahrens, M.B., Li, J.M., Orger, M.B., Robson, D.N., Schier, A.F., Engert, F., and Portugues, R. (2012). Brain-wide neuronal dynamics during motor adaptation in zebrafish. *Nature* **485**, 471–477.
- Ahrens, M.B., Orger, M.B., Robson, D.N., Li, J.M., and Keller, P.J. (2013). Whole-brain functional imaging at cellular resolution using light-sheet microscopy. *Nat. Methods* **10**, 413–420.
- Aizawa, H., Bianco, I.H., Hamaoka, T., Miyashita, T., Uemura, O., Concha, M.L., Russell, C., Wilson, S.W., and Okamoto, H. (2005). Laterotopic representation of left-right information onto the dorso-ventral axis of a zebrafish midbrain target nucleus. *Curr. Biol.* **15**, 238–243.
- Akerboom, J., Chen, T.W., Wardill, T.J., Tian, L., Marvin, J.S., Mutlu, S., Calderón, N.C., Esposti, F., Borghuis, B.G., Sun, X.R., et al. (2012). Optimization of a GCaMP calcium indicator for neural activity imaging. *J. Neurosci.* **32**, 13819–13840.
- Alivisatos, A.P., Chun, M., Church, G.M., Greenspan, R.J., Roukes, M.L., and Yuste, R. (2012). The brain activity map project and the challenge of functional connectomics. *Neuron* **74**, 970–974.
- Amo, R., Aizawa, H., Takahoko, M., Kobayashi, M., Takahashi, R., Aoki, T., and Okamoto, H. (2010). Identification of the zebrafish ventral habenula as a homolog of the mammalian lateral habenula. *J. Neurosci.* **30**, 1566–1574.
- Arrenberg, A.B., and Driever, W. (2013). Integrating anatomy and function for zebrafish circuit analysis. *Front Neural Circuits* **7**, 74.
- Baldauf, Z.B., Wang, X.-P., Wang, S., and Bickford, M.E. (2003). Pretectotectal pathway: an ultrastructural quantitative analysis in cats. *J. Comp. Neurol.* **464**, 141–158.
- Bargmann, C.I., and Marder, E. (2013). From the connectome to brain function. *Nat. Methods* **10**, 483–490.
- Beck, J.C., Gilland, E., Tank, D.W., and Baker, R. (2004). Quantifying the ontogeny of optokinetic and vestibuloocular behaviors in zebrafish, medaka, and goldfish. *J. Neurophysiol.* **92**, 3546–3561.
- Bianco, I.H., and Wilson, S.W. (2009). The habenular nuclei: a conserved asymmetric relay station in the vertebrate brain. *Philos. Trans. R. Soc. Lond. B Biol. Sci.* **364**, 1005–1020.
- Born, G., and Schmidt, M. (2004). Inhibition of superior colliculus neurons by a GABAergic input from the pretectal nuclear complex in the rat. *Eur. J. Neurosci.* **20**, 3404–3412.
- Brecha, N., and Karten, H.J. (1979). Accessory optic projections upon oculomotor nuclei and vestibulocerebellum. *Science* **203**, 913–916.
- Brockherhoff, S.E., Hurley, J.B., Janssen-Bienhold, U., Neuhauss, S.C., Driever, W., and Dowling, J.E. (1995). A behavioral screen for isolating zebrafish mutants with visual system defects. *Proc. Natl. Acad. Sci. USA* **92**, 10545–10549.
- Brockherhoff, S.E., Hurley, J.B., Niemi, G.A., and Dowling, J.E. (1997). A new form of inherited red-blindness identified in zebrafish. *J. Neurosci.* **17**, 4236–4242.
- Burgess, H.A., Johnson, S.L., and Granato, M. (2009). Unidirectional startle responses and disrupted left-right co-ordination of motor behaviors in robo3 mutant zebrafish. *Genes Brain Behav.* **8**, 500–511.
- Burrill, J.D., and Easter, S.S., Jr. (1994). Development of the retinofugal projections in the embryonic and larval zebrafish (*Brachydanio rerio*). *J. Comp. Neurol.* **346**, 583–600.
- Büttner, U., and Büttner-Ennever, J.A. (2006). Present concepts of oculomotor organization. *Prog. Brain Res.* **151**, 1–42.
- Büttner-Ennever, J.A., and Horn, A.K. (1997). Anatomical substrates of oculomotor control. *Curr. Opin. Neurobiol.* **7**, 872–879.
- Chen, C.-C., Bockisch, C.J., Bertolini, G., Olasagasti, I., Neuhauss, S.C., Weber, K.P., Straumann, D., and Huang, M.Y.-Y. (2013a). Velocity storage mechanism in zebrafish larvae. *J. Physiol.*
- Chen, T.-W., Wardill, T.J., Sun, Y., Pulver, S.R., Renninger, S.L., Baohan, A., Schreiter, E.R., Kerr, R.A., Orger, M.B., Jayaraman, V., et al. (2013b). Ultrasensitive fluorescent proteins for imaging neuronal activity. *Nature* **499**, 295–300.
- Chiappe, M.E., Seelig, J.D., Reiser, M.B., and Jayaraman, V. (2010). Walking modulates speed sensitivity in *Drosophila* motion vision. *Curr. Biol.* **20**, 1470–1475.
- Cochran, S.L., Dieringer, N., and Precht, W. (1984). Basic optokinetic-ocular reflex pathways in the frog. *J. Neurosci.* **4**, 43–57.
- Collewijn, H. (1975a). Direction-selective units in the rabbit's nucleus of the optic tract. *Brain Res.* **100**, 489–508.
- Collewijn, H. (1975b). Oculomotor areas in the rabbits midbrain and pretectum. *J. Neurobiol.* **6**, 3–22.
- Datta, S.R., Vasconcelos, M.L., Ruta, V., Luo, S., Wong, A., Demir, E., Flores, J., Balonze, K., Dickson, B.J., and Axel, R. (2008). The *Drosophila* pheromone cVA activates a sexually dimorphic neural circuit. *Nature* **452**, 473–477.
- Del Bene, F., Wyart, C., Robles, E., Tran, A., Looger, L., Scott, E.K., Isacoff, E.Y., and Baier, H. (2010). Filtering of visual information in the tectum by an identified neural circuit. *Science* **330**, 669–673.
- Dombeck, D.A., Khabbaz, A.N., Collman, F., Adelman, T.L., and Tank, D.W. (2007). Imaging large-scale neural activity with cellular resolution in awake, mobile mice. *Neuron* **56**, 43–57.
- Easter, S.S., Jr., and Nicola, G.N. (1997). The development of eye movements in the zebrafish (*Danio rerio*). *Dev. Psychobiol.* **31**, 267–276.
- Fernandes, A.M., Fero, K., Arrenberg, A.B., Bergeron, S.A., Driever, W., and Burgess, H.A. (2012). Deep brain photoreceptors control light-seeking behavior in zebrafish larvae. *Curr. Biol.* **22**, 2042–2047.
- Finger, T.E., and Karten, H.J. (1978). The accessory optic system in teleosts. *Brain Res.* **153**, 144–149.
- Friedrich, R.W., Jacobson, G.A., and Zhu, P. (2010). Circuit neuroscience in zebrafish. *Curr. Biol.* **20**, R371–R381.
- Frost, B.J., Wylie, D.R., and Wang, Y.C. (1990). The processing of object and self-motion in the tectofugal and accessory optic pathways of birds. *Vision Res.* **30**, 1677–1688.

- Gabriel, J.P., Trivedi, C.A., Maurer, C.M., Ryu, S., and Bollmann, J.H. (2012). Layer-specific targeting of direction-selective neurons in the zebrafish optic tectum. *Neuron* 76, 1147–1160.
- Georgopoulos, A.P., Schwartz, A.B., and Kettner, R.E. (1986). Neuronal population coding of movement direction. *Science* 233, 1416–1419.
- Hasson, U., Nir, Y., Levy, I., Fuhrmann, G., and Malach, R. (2004). Intersubject synchronization of cortical activity during natural vision. *Science* 303, 1634–1640.
- Huang, Y.-Y., and Neuhauss, S.C.F. (2008). The optokinetic response in zebrafish and its applications. *Front. Biosci.* 13, 1899–1916.
- Jefferis, G.S.X.E., Potter, C.J., Chan, A.M., Marin, E.C., Rohlfing, T., Maurer, C.R., Jr., and Luo, L. (2007). Comprehensive maps of Drosophila higher olfactory centers: spatially segregated fruit and pheromone representation. *Cell* 128, 1187–1203.
- Kinkhabwala, A., Riley, M., Koyama, M., Monen, J., Satou, C., Kimura, Y., Higashijima, S.-I., and Fethcho, J. (2011). A structural and functional ground plan for neurons in the hindbrain of zebrafish. *Proc. Natl. Acad. Sci. USA* 108, 1164–1169.
- Klar, M., and Hoffmann, K.-P. (2002). Visual direction-selective neurons in the pretectum of the rainbow trout. *Brain Res. Bull.* 57, 431–433.
- Kokel, D., Dunn, T.W., Ahrens, M.B., Alshut, R., Cheung, C.Y.J., Saint-Amant, L., Bruni, G., Mateus, R., van Ham, T.J., Shiraki, T., et al. (2013). Identification of nonvisual photomotor response cells in the vertebrate hindbrain. *J. Neurosci.* 33, 3834–3843.
- Lisberger, S.G. (1988). The neural basis for learning of simple motor skills. *Science* 242, 728–735.
- Lu, J., Tapia, J.C., White, O.L., and Lichtman, J.W. (2009). The interscutularis muscle connectome. *PLoS Biol.* 7, e32.
- Maimon, G., Straw, A.D., and Dickinson, M.H. (2010). Active flight increases the gain of visual motion processing in Drosophila. *Nat. Neurosci.* 13, 393–399.
- Masseck, O.A., and Hoffmann, K.-P. (2009). Comparative neurobiology of the optokinetic reflex. *Ann. N Y Acad. Sci.* 1164, 430–439.
- Mauk, M.D., and Buonomano, D.V. (2004). The neural basis of temporal processing. *Annu. Rev. Neurosci.* 27, 307–340.
- Maurer, C.M., Huang, Y.-Y., and Neuhauss, S.C.F. (2011). Application of zebrafish oculomotor behavior to model human disorders. *Rev. Neurosci.* 22, 5–16.
- McLean, D.L., Fan, J., Higashijima, S.-I., Hale, M.E., and Fethcho, J.R. (2007). A topographic map of recruitment in spinal cord. *Nature* 446, 71–75.
- Miri, A., Daie, K., Arrenberg, A.B., Baier, H., Aksay, E., and Tank, D.W. (2011a). Spatial gradients and multidimensional dynamics in a neural integrator circuit. *Nat. Neurosci.* 14, 1150–1159.
- Miri, A., Daie, K., Burdine, R.D., Aksay, E., and Tank, D.W. (2011b). Regression-based identification of behavior-encoding neurons during large-scale optical imaging of neural activity at cellular resolution. *J. Neurophysiol.* 105, 964–980.
- Muto, A., Orger, M.B., Wehman, A.M., Smear, M.C., Kay, J.N., Page-McCaw, P.S., Gahtan, E., Xiao, T., Nevin, L.M., Gosse, N.J., et al. (2005). Forward genetic analysis of visual behavior in zebrafish. *PLoS Genet.* 1, e66.
- Nagao, S. (1983). Effects of vestibulocerebellar lesions upon dynamic characteristics and adaptation of vestibulo-ocular and optokinetic responses in pigmented rabbits. *Exp. Brain Res.* 53, 36–46.
- Nestares, O., and Heeger, D.J. (2000). Robust multiresolution alignment of MRI brain volumes. *Magn. Reson. Med.* 43, 705–715.
- Neuhauss, S.C., Biehlmaier, O., Seeliger, M.W., Das, T., Kohler, K., Harris, W.A., and Baier, H. (1999). Genetic disorders of vision revealed by a behavioral screen of 400 essential loci in zebrafish. *J. Neurosci.* 19, 8603–8615.
- Niell, C.M., and Smith, S.J. (2005). Functional imaging reveals rapid development of visual response properties in the zebrafish tectum. *Neuron* 45, 941–951.
- Nikolaou, N., Lowe, A.S., Walker, A.S., Abbas, F., Hunter, P.R., Thompson, I.D., and Meyer, M.P. (2012). Parametric functional maps of visual inputs to the tectum. *Neuron* 76, 317–324.
- Northmore, D., Williams, B., and Vanegas, H. (1983). The teleostean torus longitudinalis: responses related to eye movements, visuotopic mapping, and functional relations with the optic tectum. *J. Comp. Physiol. A Neuroethol. Sens. Neural Behav. Physiol.* 150, 39–50.
- Oyster, C.W., Takahashi, E., and Collewijn, H. (1972). Direction-selective retinal ganglion cells and control of optokinetic nystagmus in the rabbit. *Vision Res.* 12, 183–193.
- Panier, T., Romano, S.A., Olive, R., Pietri, T., Sumbre, G., Candelier, R., and Debrégeas, G. (2013). Fast functional imaging of multiple brain regions in intact zebrafish larvae using Selective Plane Illumination Microscopy. *Front Neural Circuits* 7, 65.
- Pastor, A.M., De la Cruz, R.R., and Baker, R. (1994). Eye position and eye velocity integrators reside in separate brainstem nuclei. *Proc. Natl. Acad. Sci. USA* 91, 807–811.
- Portugues, R., and Engert, F. (2011). Adaptive locomotor behavior in larval zebrafish. *Front Syst Neurosci* 5, 72.
- Prochnow, N., Lee, P., Hall, W.C., and Schmidt, M. (2007). In vitro properties of neurons in the rat pretectal nucleus of the optic tract. *J. Neurophysiol.* 97, 3574–3584.
- Renninger, S.L., and Orger, M.B. (2013). Two-photon imaging of neural population activity in zebrafish. *Methods* 62, 255–267.
- Roeser, T., and Baier, H. (2003). Visuomotor behaviors in larval zebrafish after GFP-guided laser ablation of the optic tectum. *J. Neurosci.* 23, 3726–3734.
- Rohlfing, T., and Maurer, C.R., Jr. (2003). Nonrigid image registration in shared-memory multiprocessor environments with application to brains, breasts, and bees. *IEEE Trans. Inf. Technol. Biomed.* 7, 16–25.
- Ronneberger, O., Liu, K., Rath, M., Rueß, D., Mueller, T., Skibbe, H., Drayer, B., Schmidt, T., Filippi, A., Nitschke, R., et al. (2012). ViBE-Z: a framework for 3D virtual colocalization analysis in zebrafish larval brains. *Nat. Methods* 9, 735–742.
- Schrödel, T., Prevedel, R., Aumayr, K., Zimmer, M., and Vaziri, A. (2013). Brain-wide 3D imaging of neuronal activity in *Caenorhabditis elegans* with sculpted light. *Nat. Methods* 10, 1013–1020.
- Selverston, A.I. (2010). Invertebrate central pattern generator circuits. *Philos. Trans. R. Soc. Lond. B Biol. Sci.* 365, 2329–2345.
- Soodak, R.E., and Simpson, J.I. (1988). The accessory optic system of rabbit. I. Basic visual response properties. *J. Neurophysiol.* 60, 2037–2054.
- Springer, A.D., Easter, S.S., Jr., and Agronoff, B.W. (1977). The role of the optic tectum in various visually mediated behaviors of goldfish. *Brain Res.* 128, 393–404.
- Straka, H., Beck, J.C., Pastor, A.M., and Baker, R. (2006). Morphology and physiology of the cerebellar vestibulolateral lobe pathways linked to oculomotor function in the goldfish. *J. Neurophysiol.* 96, 1963–1980.
- Walls, G. (1962). The evolutionary history of eye movements. *Vision Res.* 2, 69–80.